Three-Dimensional Structures of Maturable and Abortive Capsids of Equine Herpesvirus 1 from Cryoelectron Microscopy

T. S. BAKER,[1] W. W. NEWCOMB,[2] F. P. BOOY,[3] J. C. BROWN,[2] AND A. C. STEVEN[3]*

Department of Biological Sciences, Purdue University, West Lafayette, Indiana 47907[1]; Department of Microbiology and Cancer Center, University of Virginia Health Sciences Center, Charlottesville, Virginia 22908[2]; and Laboratory of Physical Biology, National Institute of Arthritis and Musculoskeletal and Skin Diseases, Building 6, Room 114, Bethesda, Maryland 20892[3]

Cryoelectron microscopy and three-dimensional computer reconstruction techniques have been used to compare the structures of two types of DNA-free capsids of equine herpesvirus 1 at a resolution of 4.5 nm. "Light" capsids are abortive, whereas "intermediate" capsids are related to maturable intracellular precursors. Their T=16 icosahedral outer shells, ~125 nm in diameter, are indistinguishable and may be described in terms of three layers of density, totalling 15 nm in thickness. The outermost layer consists of protruding portions of both the hexon and the penton capsomers, rising ~5 nm above a midlayer of density. The innermost layer, or "floor," is a 4-nm-thick sheet of virtually continuous density except for the orifices of the channels that traverse each capsomer. Hexon protrusions are distinctly hexagonal in shape, and penton protrusions are pentagonal. The structures of the three kinds of hexons (distinguished according to their positions on the surface lattice) are closely similar but differ somewhat in their respective orientations and in the shapes of their channels. The most prominent features of the midlayer are threefold nodules ("triplexes") at the trigonal lattice points. By analogy with other viral capsids, the triplexes may represent trimers of another capsid protein, possibly VP23 (36 kilodaltons [kDa]) or VP26 (12 kDa). Intermediate capsids differ from light capsids, which are empty, in having one or more internal components. In individual images from which the shell structure has been filtered away, these components are seen to have dimensions of 20 to 30 nm but to lack a visible substructure. This material—which is smeared out in the reconstruction, implying that its distribution is not icosahedrally symmetric or necessarily consistent from particle to particle—consists of aggregates of VP22 (46 kDa). From several lines of evidence, we conclude that this protein is located entirely within the capsid shell. These aggregates may be the remnants of morphogenetic cores retained in capsids interrupted in the process of DNA packaging.

Herpesviruses form an extensive family of structurally elaborate and genetically complex viruses (for reviews, see references 14 and 21). Although they infect a wide range of host cells and are implicated in many different animal diseases, all herpesviruses conform to the same structural plan. The virion consists of a thick-walled spherical nucleocapsid, ~120 nm in diameter, enclosed within the viral envelope, and separated from it by the loosely packed, proteinaceous "tegument." Herpesvirus genomes are linear molecules of double-stranded DNA, 120 to 225 kilobase pairs in length. They are replicated in the nuclei of the host cells, in which nucleocapsids are assembled and subsequently acquire their envelopes by budding through the nuclear membrane. To date, this assembly pathway has not been mapped in detail for any herpesvirus, and little progress has been made with in vitro assembly studies. Nevertheless, evidence has been obtained in several systems that the nucleocapsid is first assembled as a DNA-free precursor capsid, into which DNA is subsequently packaged (27, 32, 36).

Several distinct types of nucleocapsid-related particles have been purified from infected cells and characterized as to their molecular constituents (22, 27, 31). In the equine herpesvirus 1 (EHV-1) system, three capsid species have been separated by density gradient centrifugation (31). The slowest-sedimenting particles, referred to as "light" capsids (lights), contain no DNA (29, 31) and have been shown, on the basis of pulse-chase experiments, to be nonmaturable (32). The particles which sediment at an intermediate position on Renografin gradients ("intermediate" capsids [intermediates]) are also devoid of DNA but contain an additional protein, VP22 (46 kilodaltons [kDa]), in about 600 copies per particle and accounting for ~10% of its mass (29, 31). Intermediates correlate with a maturable intracellular precursor (32). The fastest-sedimenting particles ("heavy" capsids [heavies]), usually a minor component, contain packaged DNA (31). Broadly analagous situations pertain in other herpesvirus systems. For example, A-capsids of herpes simplex virus type 1 (HSV-1) correspond to EHV-1 lights, B-capsids correspond to EHV-1 intermediates, and C-capsids correspond to EHV-1 heavies (22).

The morphologically distinctive herpesvirus capsid contains 162 capsomers (45) deployed according to icosahedral symmetry of triangulation class T=16. Twelve capsomers are "pentons," and the remainder are "hexons" which fall into three classes (P, E, and C), depending on their positions on the surface lattice (40) (see Fig. 4D). Ultrastructural studies have demonstrated that the hexons—viewed in two-dimensional projection and at limited resolution (~2.5 nm)—are sixfold symmetric (20, 40). A recent analysis combining particle mass measurements effected by scanning transmission electron microscopy with quantitative gel electrophoresis has established that EHV-1 hexons are hexamers of VP9 (148 kDa), the major capsid protein (29). EHV-1 capsids also contain several other proteins, in particular, VP19 (59 kDa,

~360 copies), VP23 (36 kDa, ~660 copies), and VP26 (12 kDa, ~1,300 copies) (29, 31).

Although the main significance of structural information concerning the viral capsid must relate ultimately to understanding the dynamics of virus assembly, several basic questions concerning its "static" structure are still unanswered. Where are the various minor proteins located? What are their functional implications? How do the structures of P, E, and C hexons differ? How do pentons differ from hexons? In particular, what distinguishes maturable intermediates from abortive lights? In an attempt to address these questions, we have begun to explore the potentialities of cryoelectron microscopy (7). The superior state of preservation of virus particles suspended in vitreous ice and imaged with minimal exposure techniques (1, 8, 41) provides data from which computational reconstruction techniques may be used to define native three-dimensional structures (4, 5, 18, 44). Here, we have applied these methods to compare the structures of EHV-1 lights and intermediates.

MATERIALS AND METHODS

Nomenclature. Icosahedral capsids are made up of morphological units (capsomers), each of which is surrounded by either six or five other capsomers. We use the terms hexon for the former and penton for the latter: these terms are synonymous with (but more succinct than) the previous usage of "hexavalent capsomer" and "pentavalent capsomer," respectively (35). "Hexamer" and "pentamer" refer to molecular complexes that contain six and five polypeptide chains, respectively, and, consistent with virological usage (although not general biochemical usage), these are assumed to be homo-hexamers and, respectively, homo-pentamers unless otherwise stated.

Virus growth and purification of capsids. Previously described procedures (29, 31) were employed for growth of EHV-1 and for capsid purification. In brief, monolayer cultures of L-929 cells propagated in Dulbecco modified minimal essential medium containing 8% newborn calf serum, 10% tryptose phosphate broth, and antibiotics were infected with the Kentucky A strain of EHV-1 (supplied by George Allen, University of Kentucky). Nuclei extracted from infected cells were disrupted by sonication, and light and intermediate capsid fractions were separated by density gradient centrifugation on Renografin-76 (29). Finally, the capsids were pelleted by centrifugation and suspended at 2 to 5 mg/ml in TE buffer (10 mM Tris hydrochloride [pH 7.4], 1 mM EDTA) or phosphate-buffered saline.

Cryoelectron microscopy. In a typical experiment, a 2-μl droplet of capsids suspended at ~2 mg/ml in phosphate-buffered saline was adsorbed to a thin carbon film for 10 s. The grid was briefly blotted from both sides simultaneously with filter paper to reduce the drop to a thin film and immediately plunged into liquid ethane at −180°C in the reservoir of a Reichert KF-80 cryostation (Reichert Scientific Instruments, Buffalo, N.Y.). The grid was transferred into the precooled tip of a Gatan 626 cryoholder (Gatan Inc., Warrendale, Pa.), which was then inserted into a Philips EM400T electron microscope. After waiting an appropriate interval (usually, 10 to 60 min) to allow for thermal stabilization of the cryoholder and restoration of the vacuum, we searched the grid to locate fields of particles in an ice layer of suitable thickness. During this procedure, the microscope was operated in the diffraction mode with the beam defocused to provide a low-magnification (~×2,000) image. Micrographs were recorded from suitable areas at a nominal

magnification of ×36,000 (8) and at defocus settings such that the first zero of the phase-contrast transfer function of the microscope occurred at ~(3.0 nm)⁻¹. Low-dose techniques, utilizing the Philips beam deflection unit, were used, so that the specimens imaged received exposures of 500 to 1,000 e^-/nm^2. Magnifications were calibrated according to the 2.49-nm spacing of Olive-T crystallites, and we estimate that the dimensions reported (see Results) are reliable to an accuracy of about 1%.

Image processing. (i) Digitization. Micrographs were digitized on a 50-μm raster (corresponding to 1.39 nm at the specimen) on a Colorscan C-4100 scanning microdensitometer (Optronics International Inc., Chelmsford, Mass.). The digital images were displayed on a raster graphics device (model 3400; Lexidata Corp., Billerica, Mass.), and images of individual capsids, boxed within circular boundaries, were extracted from the digitized fields. Each such image was corrected for background gradients arising from variations in the thickness of the ice layer, and the average background density was then subtracted (15). Images preprocessed in this way are referred to as "raw" images. No corrections were made for nonlinearities of the contrast transfer function, but the imaging conditions (defocus, etc.) were essentially the same for all the data analyzed.

(ii) Translational alignment and determination of orientation. The coordinates of the center of each particle and its orientation angles (θ, φ, and ω [26]) were determined by an iterative refinement procedure involving cross-correlation (16) and "common-lines" (13) methods. An initial fix on the center of the particle, more accurate than the visual estimate made during the boxing operation, was determined by a cross-correlation method (29a), in which the particle is aligned with itself after rotation through 180°. A first approximation to the viewing direction was made by searching the entire icosahedral asymmetric unit (θ = 69 to 90°; φ = −32 to 32°; ω = 0 to 180° in 1° steps), using a modified version (4, 18) of the original common-lines method (13).

Correct identification of these orientation parameters is highly dependent on a precise determination of the origin of the particle. Accordingly, after the initial orientation determination, the coordinates of the center of the particle were refined, and then the orientation parameters were refined on a finer grid (with increments of <1°). Alternate cycles of centering and orientation refinement were continued until no further improvement was detected in the phase residuals, which measure the departure of the data from icosahedral symmetry (13). Finally, the translational alignment of each image was confirmed by checking the location of the maximum of the cross-correlation function calculated between the image in question (translated into the appropriate setting) and a reference image obtained by reprojecting the reconstruction (see below) in the appropriate viewing geometry.

(iii) Three-dimensional reconstruction. Three-dimensional reconstructions were performed by Fourier-Bessel techniques (13). The three-dimensional Fourier transforms inverted to compute these reconstructions were truncated at (4.5 nm)⁻¹, the resolution limit of the data (see Results). At this spatial frequency, contrast transfer was already attenuated to a substantial extent for images in the range of defocus used, indicating that essentially all accessible information was, in fact, extracted from the micrographs. Careful application of "cross-common-lines" techniques (18) was required to bring out enantiomorphic features of the capsid structure in the reconstructions. Representations of both two- and three-dimensional density distributions were displayed on the raster graphics device and photographed with
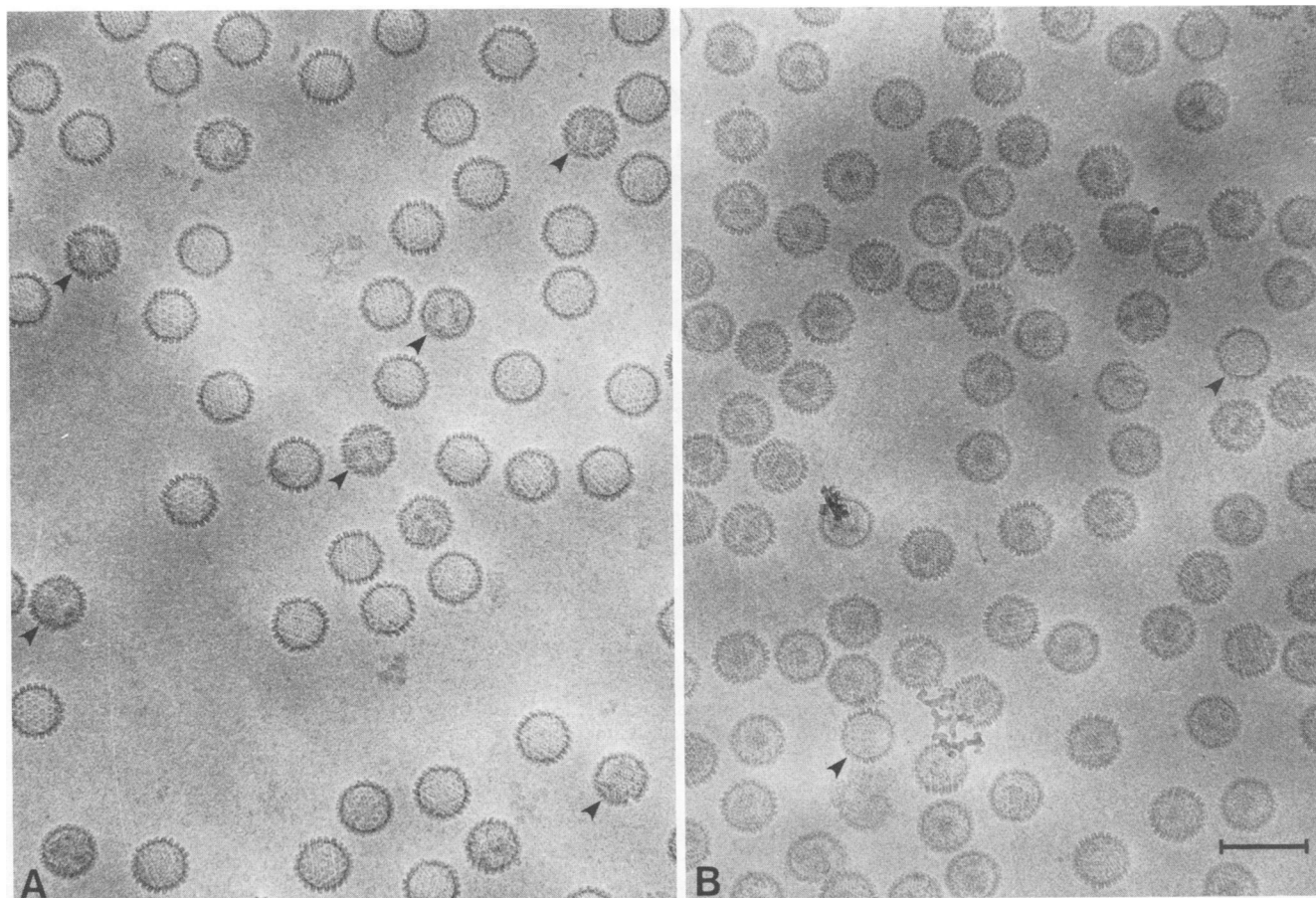
FIG. 1. Cryoelectron micrographs of EHV-1 light (A) and intermediate (B) capsids. Arrowheads identify some intermediate capsids in the light capsid preparation in panel A and vice versa in panel B. Bar, 200 nm.

a graphics recorder (model 3000; Matrix Instruments, Orangeburg, N.Y.). The contour level chosen for each shaded surface representation was the value at which the highest density gradient (local contrast) was obtained. This result was consistent with the conclusion of a more empirical approach, based on such considerations as plausible continuity of density, absence of disconnected "islands" of density, etc. All computational procedures were performed on a VAX 8550 computer (Digital Equipment Corp., Maynard, Mass.).

(iv) Filtered images of intermediate capsid "cores." Filtered images of intermediate capsid cores were computed as difference images between the raw capsid images and the corresponding "shell" images. The latter were obtained by reprojecting the intermediate capsid reconstruction (restricted to the outer shell portion thereof) in the appropriate viewing geometry. Each such pair of images was normalized by constraining them both to have the same mean and the same variance (11) within the annular region corresponding to the outer rim of the projected capsid (which is not affected by density contributions from internal components).

RESULTS

Cryoelectron microscopy. Figure 1 shows cryoelectron micrographs of light and intermediate capsids. To a first approximation, the typical light capsid appears as a uniform disk with a denser rim. On closer inspection, most particles

are found to be polyhedral rather than circular in outline, and distinct serrations are visible around their peripheries, corresponding to side views of capsomers in projection. Intermediate capsids, on the other hand, show an additional "patch(es)" of density. These patches never extend beyond the edges of the particles, implying that they represent internally located aggregates of protein. Moreover, their appearance is somewhat variable from particle to particle and, even allowing for differences in viewing angle, are not suggestive of a highly ordered internal structure (see below). This pronounced morphological distinction between the two kinds of particles allows determination of the levels of cross-contamination between the two gradient fractions (29).

Three-dimensional reconstructions. Sets of light and intermediate particles (characterized as such on the basis of the morphological distinction noted above) were digitized and used to synthesize three-dimensional reconstructions according to the common-lines procedure of Fourier analysis (4, 13, 18). Particular attention was paid to iterative refinement of the translational alignment and orientational setting of each particle and elimination of the few anomalous particles that proved to be significantly discordant with the rest of the data set. In all, 37 lights and 39 intermediates were used in the respective reconstructions. To confirm that the orientation of each particle had been correctly determined, we reprojected the reconstruction in the appropriate viewing geometry and compared it with the original image both
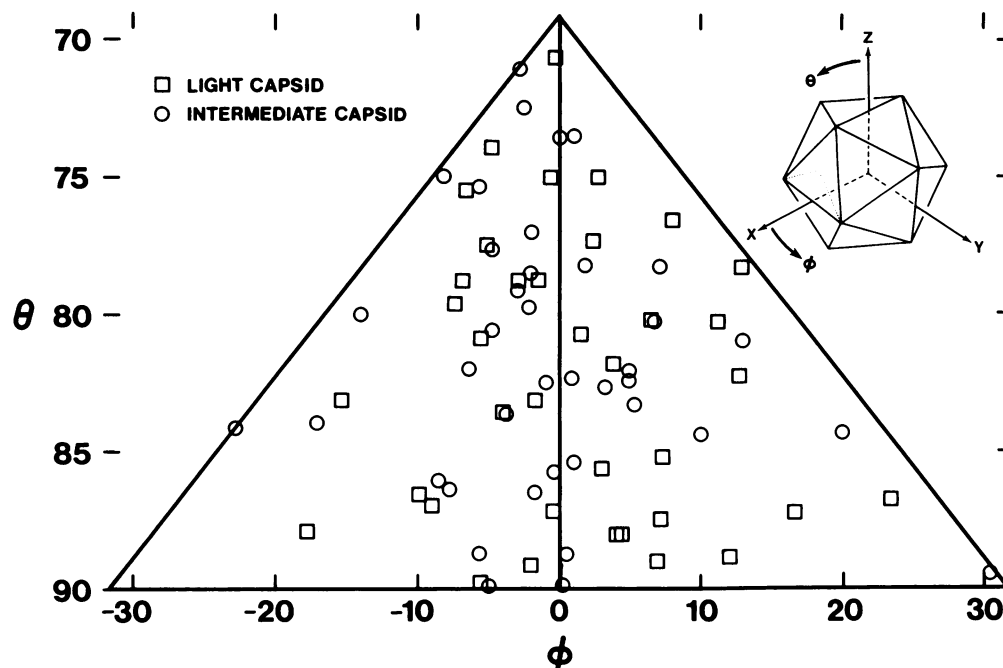
FIG. 2. Plot of the refined orientations (θ and ϕ) determined for each particle used to compute the two three-dimensional reconstructions. The orientation of each particle is mapped in the icosahedral asymmetric unit (26).

visually (see, e.g., Fig. 8) and by quantitative criteria (see Materials and Methods). The orientation of each particle used in either reconstruction is mapped in the icosahedral asymmetric unit in Fig. 2. In both cases, the orientations are distributed fairly uniformly, indicating that the views obtained were not confined to a few particular orientations; consequently, rather uniform samplings of both three-dimensional Fourier transforms were achieved.

To assess the reproducibility of the structural details revealed in the reconstructions, we arbitrarily divided each data set into two half sets, from which two independent reconstructions were calculated. In all essential features, the pairs of reconstructions thus obtained were entirely consistent both with each other and with the reconstructions obtained from the complete data set. We conclude, therefore, that sufficient data were included to ensure extraction of the maximum amount of information.

From the two three-dimensional Fourier transforms corresponding to each pair of partial reconstructions, a phase residual was calculated in equally spaced spherical shells of Fourier space. Plotting this phase residual as a function of spatial frequency (Fig. 3) provides a measure of how the consistency between the two partial reconstructions varies as one proceeds to progressively higher resolutions. This procedure is a generalization of one of the standard resolution criteria applied to sets of two-dimensional images (17). A similar residual function that also takes into account amplitude information (D. Winkelmann and T. S. Baker, unpublished results) was also calculated (data not shown). According to both criteria, a high degree of consistency was observed out to a limit of $\sim(4.5 \text{ nm})^{-1}$, at which point the phase residual crosses the threshold value of 45° (17). Accordingly, we take this figure (4.5 nm) to be the effective resolution of both reconstructions.

Structures of light and intermediate capsids. Figures 4A to C show the reconstructions, appropriately contoured and

shaded to convey the topographies of the outer surfaces of the particles and the inner surfaces of lights. A transverse "slice" of a light capsid, exposing the supramolecular envelope in cross-section, is shown in Fig. 5. This figure also shows several features whose dimensions are compiled in Table 1. To the level of detail accessible at this resolution, the outer surfaces—and indeed the entire shell structures—of lights and intermediates are indistinguishable. The shell is 14.1 to 15.0 nm thick (Table 1) and may be described in terms of three layers. The outermost layer consists of hollow "protrusions" at the hexon sites and, slightly less prominently, also at the penton sites. The hexon protrusions exhibit pronounced sixfold symmetry, and the penton pro-
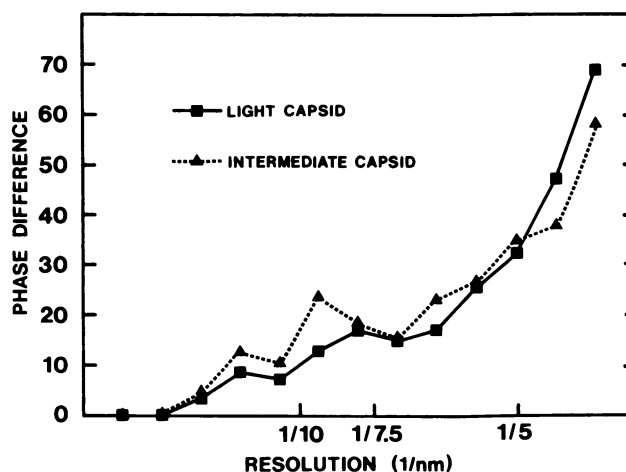

FIG. 3. Plot of a phase residual as a function of resolution between two independent reconstructions each of light and intermediate EHV-1 capsids.
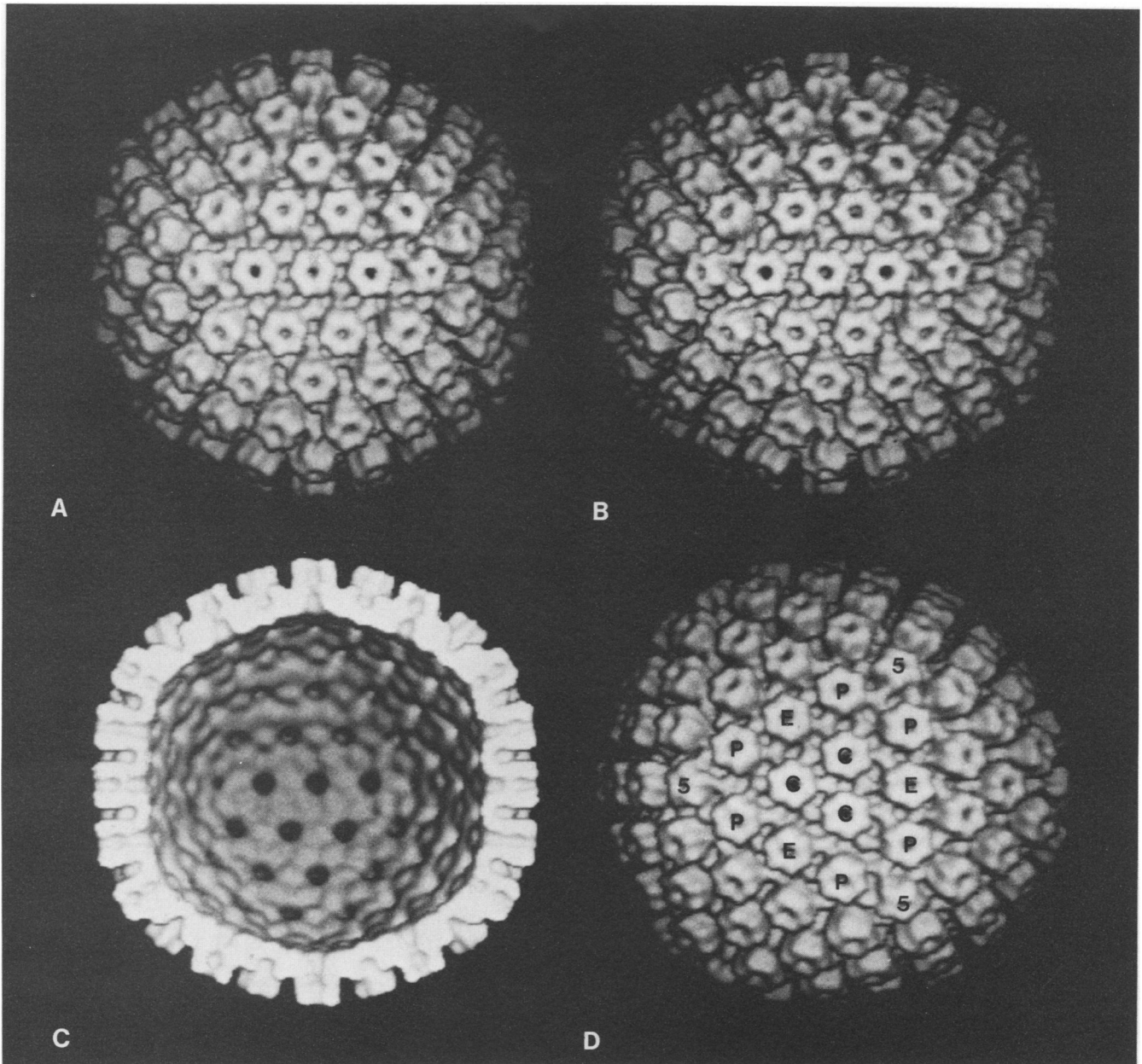
FIG. 4. Surface-shaded representations of the outer surfaces of light (A) and intermediate (B) capsids, viewed along a twofold axis of icosahedral symmetry. Also shown is the inner surface of the light capsid reconstruction (C): the same morphological features were revealed inside the intermediate capsid, which also contained additional, internal density that was smeared out in the reconstruction, indicating a nonsymmetric distribution in individual particles (see Results). Panel D shows a threefold view, marking the four kinds of capsomers present on the T=16 capsid surface lattice: P, peripentonal hexon; E, edge hexon; C, center hexon; 5, penton.

trusions are fivefold symmetric. The six components of each hexon protrusion are slightly slewed, i.e., tilted relative to the radial vector emanating from the center of the particle (3); moreover, the orientation of the hexon protrusion relative to the surface lattice lines is slightly skewed.

The dominant features of the midlayer are trimeric concentrations of density ("triplexes"), ~5 nm in diameter, at the trigonal positions. The three tips of each triplex appear to merge into the sides of the surrounding hexagonal protrusions, although this connectivity may as well represent an effect of the limited resolution as genuine continuity of density.

Finally, the innermost layer ("floor") consists of a sheet of almost continuous density, ~4 nm thick, giving an inner surface that is smooth and featureless except for the indentations that underlie each capsomer (Fig. 4C). These indentations are much wider at hexon sites than at penton sites (Table 1). Viewed in cross-section (Fig. 5), they are seen to be the orifices of channels that run through the center of each capsomer. These central channels are nonuniform in bore, having two constrictions, one of which (the narrower) is located approximately halfway through the shell and the other of which is located just inside the external orifice of the channel. Interestingly, the shape of this channel is the
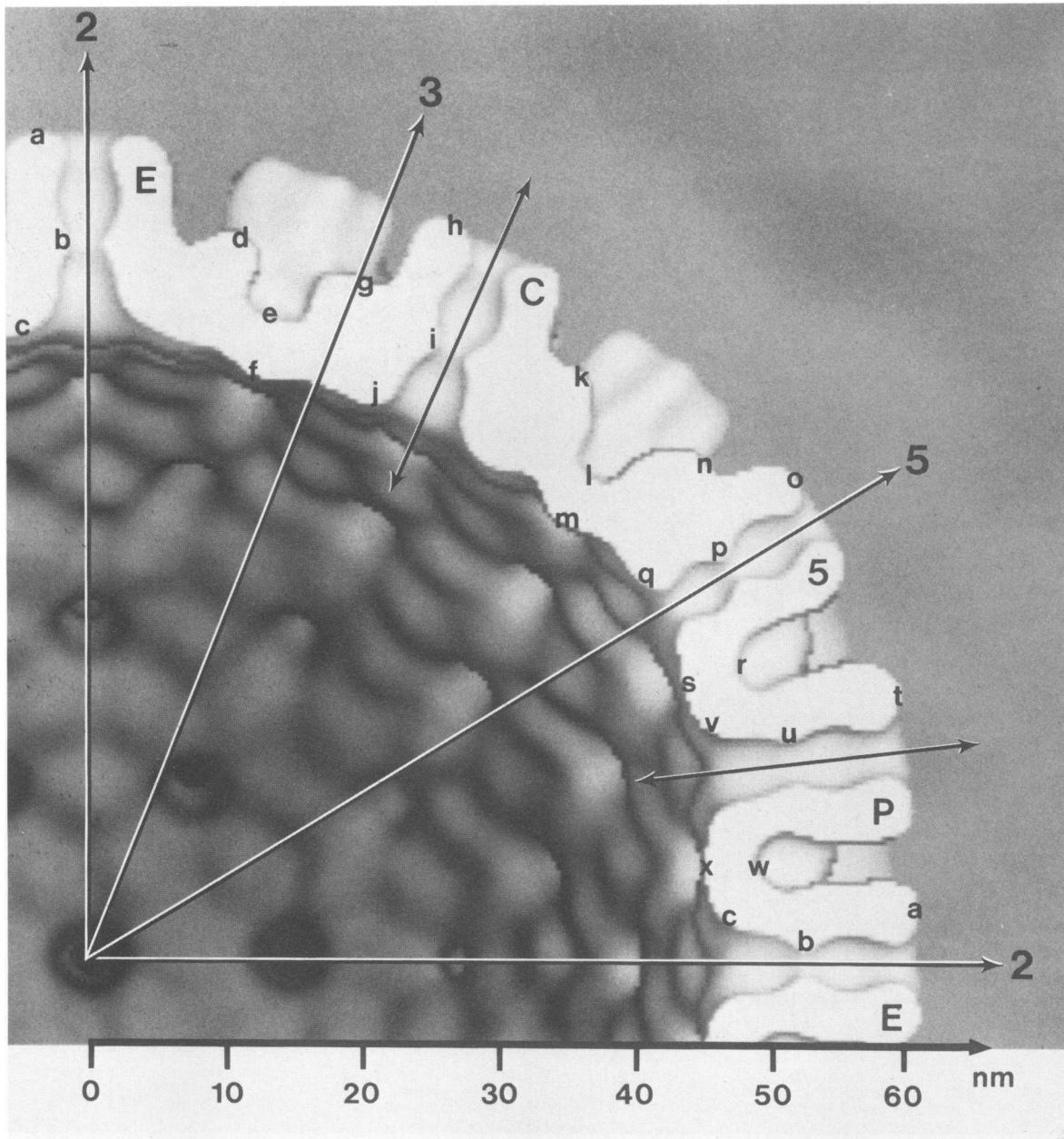
FIG. 5. Octant of EHV-1 light reconstruction, viewed along an icosahedral twofold axis of symmetry and sliced along an equatorial plane in which the icosahedral two-, three-, and fivefold symmetry axes (normal to the viewing direction) lie. All capsomers have prominent channels which connect the capsid interior with the external milieu. Their bore is distinctly nonuniform, but its value at any given radial position is somewhat sensitive to the choice of contour level, so that it is not possible to make a precise estimate for an exclusion limit for these channels. A narrowing of the channel near the center and also towards the external surface is observed in all four types of capsomers. Abbreviations are as in Fig. 4.

feature that shows the greatest variation among hexons of types P, E, and C (Fig. 5 and 4D). The inner surface of the intermediate capsid shell does not differ from that of the light capsid shell in any significant respect (data not shown).

The capsomeric substructure is illustrated in Fig. 6 in planar slices from two different radial levels for pentons as well as for all three hexons. These sections emphasize the sixfold symmetry (and, respectively, fivefold symmetry) and skewness of the external protrusions and bring out the triplexes that are located both between triplets of hexons and between pentons and pairs of type P hexons (Fig. 6).

To convey the overall distribution of mass, we calculated a spherically averaged radial density distribution from each reconstruction (Fig. 7). In the shell, the two curves are essentially superimposable and clearly demonstrate the three strata (protrusions, midlayer, and floor) discussed above. Inside the shell, the intermediate density profile systematically overlies that of the lights, thus revealing the presence of additional material inside intermediates.

Internal components of intermediate capsids. The structures of the patches of internal density present in intermediate capsids are difficult to infer from individual images of

TABLE 1. Radial distances to structural features of the EHV-1 light capsid[a]

Capsomer	Radial distance (nm) to:						
	Outer tip of protrusion	Major channel constriction	Base (inner surface)	Outer tip of triplex	Top surface of pit	Inner surface of pit	Tip of triplex (next)
E hexon	61.3 (a)	53.0 (b)	46.5 (c)	55.1 (d)	49.6 (e)	45.2 (f)	54.6 (g)
C hexon	61.1 (h)	52.5 (i)	46.2 (j)	57.2 (k)	51.7 (l)	47.5 (m)	59.0 (n)
P hexon	63.7 (t)	54.3 (u)	48.8 (v)		49.9 (w)	46.5 (x)	
Penton	64.0 (o)	56.4 (p)	49.9 (q)		53.0 (r)	48.8 (s)	

[a] The letters in parentheses refer to sites marked in Fig. 5. The pit denotes the broadening of the transcapsomer channel as it approaches the inner surface of the capsid shell. The outer diameters of the capsid are 127.9 nm between tips of opposing pentons and 127.4 nm between tips of opposing P hexons. These figures are quite close because the greater radial excursion of the vertex site of the penton is largely offset by the greater height of the hexon (14.9 nm, base to tip, as compared with 14.1 nm for the penton). The average thickness of the capsid floor, calculated as (ef + lm + ra + wx)/4, is 4.0 nm.

intermediate capsids, at least in part because they are viewed in coprojection with the shell structure. However, our reconstruction may be used to "peel off" the shell contribution and thus expose the internal components. This operation was performed for each particle included in the intermediate reconstruction, and several examples of core projection images are compiled in Fig. 8B to F. Figure 8A shows a similar analysis for a light capsid, considered as a control experiment: the resulting difference image is featureless noise. Taken together, the core images of intermediate capsids do not suggest a set of different views of a regular structure that is uniform from particle to particle but rather reveal that each intermediate contains a roundish coagulate (or coagulates) of density, some 20 to 30 nm in extent.

The amount of projected density associated with these features was integrated in each case and compared with the mass (cumulative projected density) of the shell. Expressed as a fraction of the total capsid mass, the core contribution averaged 10.4% (standard deviation, ±4.9%; range, 2.5 to 19.5%; $n = 36$, with three seemingly anomalous particles

omitted from consideration). We consider it likely that these figures represent some variability in core content from particle to particle, as well as the uncertainty implicit in the calculations.

DISCUSSION

Although limited in scope, currently available information is consistent with the proposition that the nucleocapsid assembly pathways of EHV-1, HSV-1, and cytomegalovirus proceed along broadly similar lines; accordingly, our findings will be discussed in relation to other data pertaining to all three herpesvirus systems. First (as with DNA-containing bacteriophages [6, 23]), a precursor capsid is assembled which contains no DNA but does contain a protein (or proteins) that is, in large part, removed as this particle matures into a genome-containing capsid (27, 32, 33, 36). Abortive empty capsids that contain neither these proteins nor DNA (A-capsids, lights) are not assembled on a different pathway from viable precursors (B-capsids, intermediates)
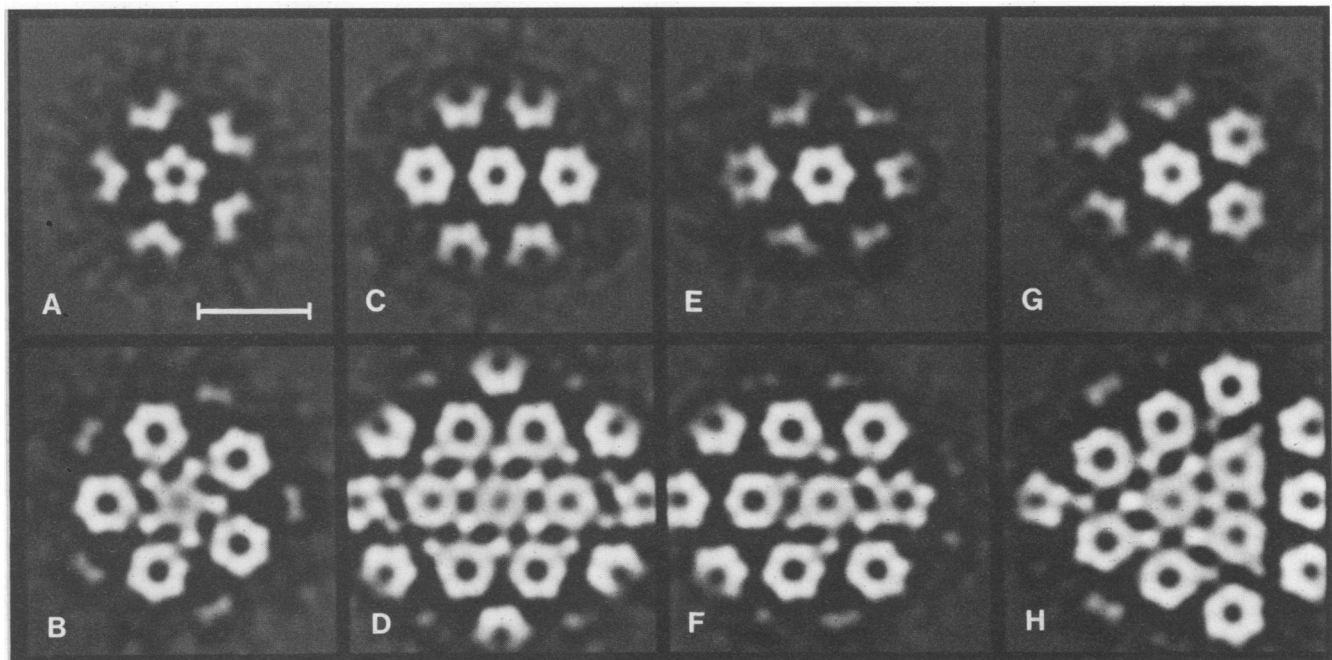

FIG. 6. Cross-sectional views perpendicular to the axes of the four different types of capsomers. These computationally derived sections show slices excised from the complete light reconstruction. The top row shows sections through the region of maximum density in the external protrusion of each capsomer, at radii (in nanometers) of 60.4 (A), 58.3 (C), 59.7 (E), and 59.0 (G). The bottom row shows sections at a level at which the transcapsomer channels are narrowest, at radii (in nanometers) of 56.2 (B), 52.8 (D), 54.9 (F), and 52.8 (H). Bar, 25 nm.
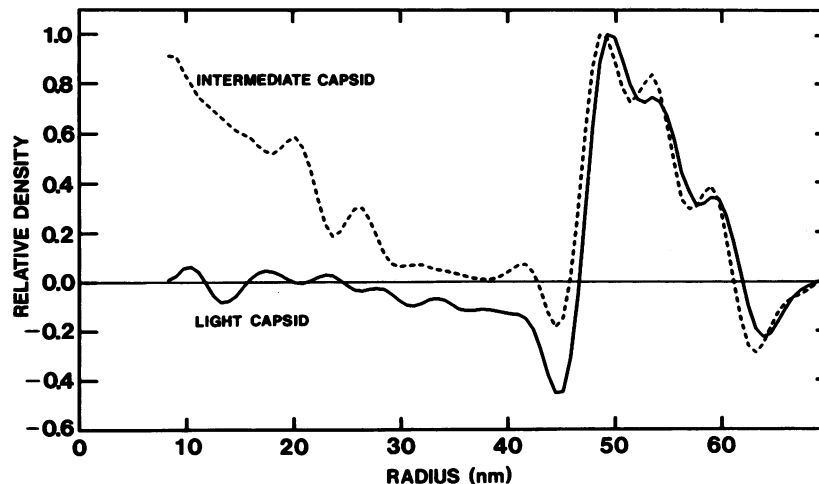
FIG. 7. Spherically averaged radial density distributions calculated from the light and intermediate reconstructions.

but rather are generated from them when packaging miscarries in such a way that the transient proteins are lost without effecting a secure packaging of DNA.

The reconstructions described here substantiate and clarify earlier inferences based on electron microscopy of negatively stained and shadowed preparations. Moreover, our rendition of the EHV-1 light capsid has much in common with the recent reconstruction of HSV-1 A-capsids by Schrag et al. (37). Some discrepancies exist, however, with regard to the following points: (i) our radial density profile resolves three, not two, distinct layers of density in the capsid shell (cf. our Fig. 7 with Fig. 5 in Schrag et al. [37]); (ii) the hexon protrusions in our reconstructions (Fig. 3) are distinctly hexagonal, in comparison with the relatively annular morphology of those shown by Schrag et al. (37); and (iii) the appearances of the respective pentons are also significantly different (cf. our Fig. 3 with Fig. 2 in Schrag et al. [37]).

Hexon structure. From the three-dimensional structure, it is apparent that the pronounced sixfold symmetry previously demonstrated for hexons in projection (20, 30, 40) is due primarily to their external protrusions. P, E, and C hexons are quite similar in overall morphology, although significant differences were observed in the shapes of their respective channels, which are widest in E hexons and narrowest in P hexons. Such differences can be generated by slight changes in slew displacement between the six subunits that surround a channel, as pointed out in consideration of the gap junction connexon (42): possibly, a similar mechanism is involved in accommodating VP9 subunits in quasiequivalent sites on EHV-1 capsids.

After capsid polymerization is complete, DNA must be packaged into this preformed receptacle. During this process, some proteins are expelled from the precursor capsid (27). Subsequently, DNA must be released from the capsid in the next cycle of infection. Since our reconstructions
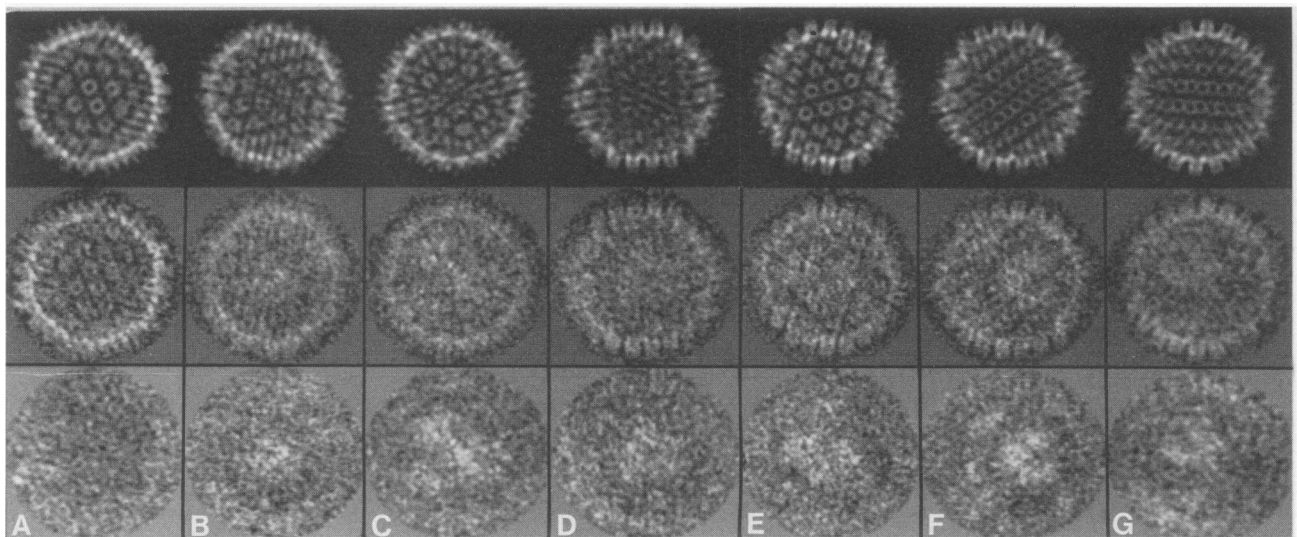

FIG. 8. Computer filtering of cryoelectron micrographs of intermediate capsids, revealing their internal core structures, which are aggregates of VP22. In each case, the reconstruction was reprojected into the appropriate viewing angle and the projected density distribution of the shell was computationally subtracted from the original image to expose the internal structures. Panel A shows the same analysis for a light capsid, which has no internal components.

show a shell structure which seals off the capsid interior from the external milieu except for the transcapsomer channels, the channels clearly afford the most obvious pathways for these transfer reactions to take place. On the grounds of relative ease of achieving a completely internalized but unbroken genome, we note that packaging is likely to involve only a single channel on any given capsid. If this channel were to be selected at random, then some mechanism would be required to prevent packaging from being initiated at other capsomer channels. On the other hand, some subtle structural feature might distinguish a singular capsomer destined to be the packaging site. In this case, however, one would not expect such a feature to be visualized in our reconstructions, since it would be smeared out in symmetry-related averaging.

Penton structure. EHV-1 pentons have a well-defined fivefold symmetry (Fig. 3 and 6). A question of acute interest is whether they are pentamers of VP9—in keeping with the tenets of quasiequivalence theory (12)—or of some other viral protein, as has turned out to be the case for adenovirus (10) and T-even bacteriophages (6). The morphological features discernible at the present resolution are generally consistent with the former possibility (Fig. 3 and 6). Thus, if the pentons were pentamers of a different protein, its molecular weight would be similar to that of VP9 (although the possibility is not ruled out that a complex of comparable size could be made up from a larger number of smaller subunits [37]) and it would account for 3 to 4% of the capsid mass. Gel analysis shows no obvious candidate for such a protein (29). On the other hand, several observations indicate that pentons are markedly more susceptible to proteolysis than hexons. Mild trypsinization of HSV-2 capsids has the effect of excavating penton sites (40). Three-dimensional reconstructions of cryoimages of proteolyzed HSV-1 capsids have revealed extensive holes at the penton sites together with seemingly intact hexons (R. H. Vogel, W. W. Newcomb, J. C. Brown, F. P. Booy, and A. C. Steven, unpublished results). This differential susceptibility to proteolysis implies that pentons may consist of a different protein (or proteins) than hexons, although these observations might otherwise be accounted for by the same protein having (in pentons) a somewhat different folding and a more exposed capsid site. We conclude that the present data are insufficient to settle the molecular identity of the pentons.

Are triplexes trimers of a minor capsid protein? For both lights and intermediates, the threefold nodules between adjacent triplets of capsomer protrusions are the most prominent features of the capsid midlayer and may correlate with the "inter-capsomeric fibrils" reported by Vernon et al. (43). For comparison, it is noteworthy that the capsids of T-even (2, 25, 39) and lambda (24, 46) bacteriophages both have trimers of a small protein overlying the threefold positions between hexamers of their major capsid proteins. These accessory proteins, called *soc* (11 kDa, T-even) and gpD (10 kDa, lambda), bind to their respective capsids subsequent to the completion of assembly; their roles are to provide structural reinforcement. Furthermore, trimers of the adenovirus protein IX (14 kDa) have recently been mapped at certain threefold sites between hexons (10, 19) on its outer capsid surface. Although current evidence is insufficient to rule out the possibility that EHV-1 triplexes are domains of VP9 molecules, the hypothesis that they are trimers of some other protein is strongly favored by analogy with these other viral systems. The most likely candidates are VP23 (see also Schrag et al. [37]) and VP26, the 12-kDa minor capsid protein.

VP22 is located inside EHV-1 intermediate capsids. Chemically, intermediates differ from lights in that they are ~10% more massive, on account of an additional protein, VP22, which is present, on average, at about 600 copies per particle (29). Since neither capsid has any significant amount of DNA and since they have the same dimensions, it is presumably the presence of VP22 that accounts for the more rapid sedimentation of intermediates than of lights in density gradients. Cryoimages of intermediates show clumps of density that are not present in lights (cf. Fig. 1A and B) and that correlate with the presence of VP22. Several lines of evidence concur that these clumps are located entirely within the capsid shell. First, in unprocessed images (e.g., Fig. 1), they are never seen to protrude beyond the capsid shell periphery. Second, the outer surfaces of lights and intermediates as conveyed in the respective reconstructions are indistinguishable (cf. Fig. 4A and B). Third, the radial density profiles (Fig. 7) show additional density lying inside the intermediate capsid shell. Fourth, when the shell contribution is separated from that of the core component (Fig. 8) and their respective densities are integrated, the core mass averages 10% of the total capsid mass, which tallies with the amount of VP22 determined independently by scanning transmission electron microscopic mass analysis (29). We conclude, therefore, that these clumps are aggregates of VP22 located inside the capsid shell and that no detectable amount of this protein is located on its external surface. Assuming that VP22 is the counterpart of VP22a of HSV-1, these results contradict the external localization attributed to this protein by Braun et al. (9) and Sherman and Bachenheimer (38). They are, however, in accord with the recent ion-etching studies of Newcomb and Brown (28), which indicated that VP22a is located inside the HSV-1 capsid shell.

Other minor capsid proteins. The other capsid proteins, notably VP19, are presumably integral components of the capsid shell and closely associated with VP9, although we have little information on which to base a more specific localization. Qualitatively, there is a close resemblance between the respective compositions of EHV-1 lights and A-capsids of HSV-1, in that both seem to have essentially the same set of minor proteins at similar molecular weights (22, 29). Quantitatively, however, some of these proteins are considerably more abundant in A-capsids, and this distinction may provide a basis on which to localize them, assuming that they occupy the same berths in both systems (i.e., structural features associated with them should be relatively enhanced in capsids in which they are present in greater numbers).

Proteinaceous cores in maturable capsids. One such protein is VP22, whose counterparts (called p40, ICP35, or VP22a) in HSV-1 and cytomegalovirus are two to four times more abundant in isolated B-capsids than VP22 is in EHV-1 intermediates (22, 29). In HSV-1, a *ts* mutant has been obtained which, at nonpermissive temperatures, stockpiles intracellular capsids with distinctive internal structures (34), and similar particles accumulate in cytomegalovirus infections in which DNA packaging is inhibited by hydroxyurea (27). Thin-section electron micrographs suggest that these structures are substantial in content and highly ordered— possibly spherically or icosahedrally symmetric. In contrast, the VP22 aggregates in EHV-1 intermediates do not appear to be highly ordered structures (Fig. 8): moreover, they do not seem to be identical from particle to particle. Usually a single such aggregate is seen, although one often sees multiple aggregates (7; Fig. 1; also, additional data not

shown) which, in exceptional cases, are distributed with an approximate regularity.

Several explanations may account for these divergent observations. There may simply be a basic difference between the proteinaceous structures inside maturable precursor capsids in the respective herpesvirus systems. Alternatively, these internal core structures may be labile, and although those inside EHV-1 intermediates are initially like those in intracellular HSV-1 (36) and cytomegalovirus (27) capsids, they are broken down and partially lost during isolation. However, a third and more intriguing explanation may also apply. In a normal infection, a fully assembled capsid precursor with a complete morphogenetic core is likely to be short-lived and subject to structural changes upon the onset of DNA packaging. This step would, however, be blocked at nonpermissive temperatures for packaging-deficient mutants (36) or by hydroxyurea treatment (27), leading to an accumulation of fully cored precursor capsids. In terms of this hypothesis, EHV-1 intermediates would be expected to represent heterogeneous populations of particles interrupted at various stages of DNA packaging. Accordingly, their morphogenetic cores would be reorganized and partially eliminated to various degrees. This explanation certainly accounts both for their variability and for their difference from intracellular capsids inhibited from DNA packaging (see above). To account for the negligible DNA content of purified intermediates, we must further postulate that partially packaged DNA is not securely associated with these capsids and is easily detached during isolation.

ACKNOWLEDGMENTS

LITERATURE CITED

1. Adrian, M., J. Dubochet, J. Lepault, and A. McDowell. 1984. Cryo-electron microscopy of viruses. Nature (London) 308: 32–36.

2. Aebi, U., R. van Driel, R. K. L. Bijlenga, B. ten Heggeler, R. van der Broek, A. C. Steven, and P. R. Smith. 1977. Capsid fine structure of T-even bacteriophages. Binding and localization of two dispensable capsid proteins into the P23 surface lattice. J. Mol. Biol. 110:687–698.

3. Baker, T. S., D. L. D. Caspar, C. J. Hollingshead, and D. A. Goodenough. 1983. Gap junction structures. IV. Asymmetric features revealed by low-irradiation microscopy. J. Cell Biol. 96:204–216.

4. Baker, T. S., J. Drak, and M. Bina. 1988. Reconstruction of the three-dimensional structure of simian virus 40 and visualization of the chromatin core. Proc. Natl. Acad. Sci. USA 85:422–426.

5. Baker, T. S., J. Drak, and M. Bina. 1989. The capsid of small papova viruses contains 72 pentameric capsomeres: direct evidence from cryo-electron microscopy of simian virus 40. Biophys. J. 55:243–253.

6. Black, L. W., and M. K. Showe. 1983. Morphogenesis of the T4 head, p. 219–245. In C. K. Mathews, E. M. Kutter, G. Mosig, and P. B. Berget (ed.), Bacteriophage T4. American Society for Microbiology, Washington, D.C.

7. Booy, F. P., W. W. Newcomb, J. C. Brown, and A. C. Steven. 1988. Herpesvirus nucleocapsids visualized in the frozen-hydrated state. Proceedings of the 46th Annual Meeting of the Electron Microscopy Society of America, p. 164–165. San Francisco Press, San Francisco.

8. Booy, F. P., R. W. H. Ruigrok, and E. F. J. van Bruggen. 1985.

Electron microscopy of influenza virus. A comparison of negatively stained and ice-embedded particles. J. Mol. Biol. 184: 667–676.

9. Braun, D. K., B. Roizman, and L. Pereira. 1984. Characterization of post-translational products of herpes simplex virus gene 35 proteins binding to the surfaces of full capsids but not empty capsids. J. Virol. 49:142–153.

10. Burnett, R. M. 1984. Structural investigations of hexon, the major capsid protein of adenovirus, p. 337–385. In F. A. Jurnak and A. McPherson (ed.), Biological macromolecules and assemblies, vol. 1. Virus structures. John Wiley & Sons, Inc., New York.

11. Carrascosa, J. L., and A. C. Steven. 1978. A procedure for evaluation of significant structural differences between related arrays of protein molecules. Micron 9:199–206.

12. Caspar, D. L. D., and A. Klug. 1962. Physical principles in the construction of regular viruses. Cold Spring Harbor Symp. Quant. Biol. 27:1–32.

13. Crowther, R. A. 1971. Procedures for three-dimensional reconstruction of spherical viruses by Fourier synthesis from electron micrographs. Proc. R. Soc. London B 261:221–230.

14. Dargan, D. J. 1986. The structure and assembly of herpesviruses, p. 359–437. In J. R. Harris and R. W. Horne (ed.), Electron microscopy of proteins, vol. 5. Virus structure. Academic Press, Inc. (London), Ltd., London.

15. DeRosier, D. J., and P. B. Moore. 1970. Reconstruction of three-dimensional images from electron micrographs of structures with helical symmetry. J. Mol. Biol. 52:355–369.

16. Frank, J. 1980. The role of correlation techniques in computer image processing. Curr. Top. Phys. 13:187–222.

17. Frank, J., A. Verschoor, and M. Boublik. 1981. Computer averaging of electron micrographs of 40S ribosomal subunits. Science 214:1353–1355.

18. Fuller, S. 1987. The T=4 envelope of Sindbis virus is organized by interactions with a complementary T=3 capsid. Cell 48: 923–934.

19. Furcinitti, P. S., J. van Oostrum, J. S. Wall, and R. M. Burnett. 1987. Visualization of a small polypeptide within an adenovirus capsid fragment by subtracting the hexon X-ray structure from STEM images. Proceedings of the 4th Annual Meeting of the Electron Microscopy Society of America, p. 738–739. San Francisco Press, San Francisco.

20. Furlong, D. 1978. Direct evidence for 6-fold symmetry of the herpesvirus hexon capsomers. Proc. Natl. Acad. Sci. USA 75:2764–2766.

21. Hay, J., C. R. Roberts, W. T. Ruyechan, and A. C. Steven. 1987. Herpesviridae, p. 391–405. In M. V. Nermut and A. C. Steven (ed.), Animal virus structure. Elsevier Science Publishers, Amsterdam.

22. Heine, J. W., R. W. Honess, E. Cassai, and B. Roizman. 1974. Proteins specified by herpes simplex virus. XII. The virion polypeptides of type 1 strains. J. Virol. 14:640–651.

23. Hendrix, R. 1985. Shape determination in virus assembly: the bacteriophage example, p. 169–204. In S. Casjens (ed.), Virus structure and assembly. Jones and Bartlett, Boston.

24. Imber, R., A. Tsugita, M. Wurtz, and T. Hohn. 1980. The outer surface protein of bacteriophage lambda. J. Mol. Biol. 139: 277–295.

25. Ishii, T., and M. Yanagida. 1975. Molecular organization of the shell of T-even bacteriophage head. J. Mol. Biol. 97:655–660.

26. Klug, A., and J. T. Finch. 1968. Structure of viruses of the papilloma-polyoma type. IV. Analysis of tilting experiments in the electron microscope. J. Mol. Biol. 31:1–12.

27. Lee, J. Y., A. Irmiere, and W. Gibson. 1988. Primate cytomegalovirus assembly: evidence that DNA packaging occurs subsequent to B-capsid assembly. Virology 167:87–96.

28. Newcomb, W. W., and J. C. Brown. 1989. Use of Ar$^+$ plasma etching to localize structural proteins in the capsid of herpes simplex virus type 1. J. Virol. 63:4697–4702.

29. Newcomb, W. W., J. C. Brown, F. P. Booy, and A. C. Steven. 1989. Nucleocapsid mass and capsomer protein stoichiometry in equine herpesvirus 1: scanning transmission electron microscopic study. J. Virol. 63:3777–3783.

29a. Olson, N. H., and T. S. Baker. 1989. Magnification calibration and the determination of spherical virus diameters using cryo-microscopy. Ultramicroscopy 30:281–297.

30. Palmer, E. L., M. L. Martin, and G. W. Gary, Jr. 1975. The ultrastructure of disrupted herpesvirus nucleocapsids. Virology 65:260–265.

31. Perdue, M. L., J. C. Cohen, M. C. Kemp, C. C. Randall, and D. J. O'Callaghan. 1975. Characterization of three species of nucleocapsids of equine herpes virus type 1. Virology 64:187–205.

32. Perdue, M. L., J. C. Cohen, C. C. Randall, and D. J. O'Callaghan. 1976. Biochemical studies on the maturation of herpesvirus nucleocapsid species. Virology 74:194–208.

33. Perdue, M. L., M. C. Kemp, C. C. Randall, and D. J. O'Callaghan. 1974. Studies of the molecular anatomy of the L-M cell strain of equine herpes virus type 1: proteins of the nucleocapsid and intact virion. Virology 59:201–216.

34. Preston, V. G., J. A. V. Coates, and F. J. Rixon. 1983. Identification and characterization of a herpes simplex virus gene product required for encapsidation of virus DNA. J. Virol. 45:1056–1064.

35. Rayment, I., T. S. Baker, D. L. D. Caspar, and W. T. Murakami. 1982. Polyoma virus capsid structure at 22.5A resolution. Nature (London) 295:110–115.

36. Rixon, F. J., A. M. Cross, C. Addison, and V. G. Preston. 1988. The products of herpes simplex virus gene UL26 which are involved in DNA packaging are strongly associated with empty but not with full capsids. J. Gen. Virol. 69:2879–2891.

37. Schrag, J. D., B. V. Venkataram Prasad, F. J. Rixon, and W. Chiu. 1989. Three-dimensional structure of the HSV1 nucleo-capsid. Cell 56:651–660.

38. Sherman, G., and S. L. Bachenheimer. 1988. Characterization of intranuclear capsids made by morphogenetic mutants of HSV-1. Virology 163:471–480.

39. Steven, A. C., E. Couture, U. Aebi, and M. K. Showe. 1976. Structure of T4 polyheads. II. A pathway of polyhead transformations as a model for T4 capsid maturation. J. Mol. Biol. 106:187–221.

40. Steven, A. C., C. R. Roberts, J. Hay, M. E. Bisher, T. Pun, and B. L. Trus. 1986. Hexavalent capsomers of herpes simplex virus type 2: symmetry, shape, dimensions, and oligomeric status. J. Virol. 57:578–584.

41. Stewart, M., and G. Vigers. 1986. Electron microscopy of frozen-hydrated biological material. Nature (London) 319:631–636.

42. Unwin, P. N. T., and G. Zampighi. 1980. Structure of the junction between communicating cells. Nature (London) 283:545–549.

43. Vernon, S., W. Lawrence, and G. Cohen. 1974. Morphological components of herpesvirus. I. Intercapsomeric fibrils and the geometry of the capsid. Intervirology 4:237–248.

44. Vogel, R. H., S. W. Provencher, C.-H. von Bonsdorff, M. Adrian, and J. Dubochet. 1986. Envelope structure of Semliki Forest virus reconstructed from cryo-electron micrographs. Nature (London) 320:533–535.

45. Wildy, P., W. C. Russell, and R. W. Horne. 1960. The morphology of herpes virus. Virology 12:204–222.

46. Wurtz, M., J. Kistler, and T. Hohn. 1975. Surface structure of in vitro assembled bacteriophage lambda polyheads. J. Mol. Biol. 101:39–56.